ARTICLES

Quantum ground state and single-phonon control of a mechanical resonator

A. D. O'Connell[1], M. Hofheinz[1], M. Ansmann[1], Radoslaw C. Bialczak[1], M. Lenander[1], Erik Lucero[1], M. Neeley[1], D. Sank[1], H. Wang[1], M. Weides[1], J. Wenner[1], John M. Martinis[1] & A. N. Cleland[1]

Quantum mechanics provides a highly accurate description of a wide variety of physical systems. However, a demonstration that quantum mechanics applies equally to macroscopic mechanical systems has been a long-standing challenge, hindered by the difficulty of cooling a mechanical mode to its quantum ground state. The temperatures required are typically far below those attainable with standard cryogenic methods, so significant effort has been devoted to developing alternative cooling techniques. Once in the ground state, quantum-limited measurements must then be demonstrated. Here, using conventional cryogenic refrigeration, we show that we can cool a mechanical mode to its quantum ground state by using a microwave-frequency mechanical oscillator—a 'quantum drum'—coupled to a quantum bit, which is used to measure the quantum state of the resonator. We further show that we can controllably create single quantum excitations (phonons) in the resonator, thus taking the first steps to complete quantum control of a mechanical system.

The bizarre, often counterintuitive, predictions of quantum mechanics have been observed in atomic-scale, optical and electrical systems. Efforts to demonstrate that quantum mechanics also applies to a mechanical system, especially one that can be seen with the naked eye, have generated significant interest[1–13]. Most approaches focus on measuring the behaviour of a single mechanical resonance. Cooling a mechanical resonance, also called a mode, to its quantum ground state is typically an enormous challenge, as it requires temperatures $T \ll hf/k_B$, where f is the mode frequency and h and k_B are respectively Planck's and Boltzmann's constants. An audio-frequency mode at $f = 1$ kHz, for example, would need to be cooled to $T \ll 50$ nK. However, the resonant frequency scales inversely with the size of the system, with higher characteristic frequencies in smaller systems. Researchers have therefore pursued combinations of very small mechanical resonators together with novel cooling techniques[14–18]. The use of nanomechanical resonators, with mode frequencies in the megahertz band, eases the stringent temperature requirements, and when combined with quantum-optics-based refrigeration has allowed a number of demonstrations of near-quantum-limited behaviour[19–22].

Here we use conventional cryogenic refrigeration to cool a mechanical mode to its quantum ground state. We achieve this by using a micromechanical resonator[5] with an isolated mechanical mode near 6 GHz, which we term a microwave-frequency 'quantum drum', whose ground state is reached for temperatures below ~0.1 K. Such temperatures can easily be reached using a dilution refrigerator. We perform quantum-limited measurements of the resonator using a superconducting quantum bit (or qubit), an electronic device developed for quantum computation[23,24]. Coupling such a quantum device to the resonator should allow completely quantum-coherent measurements, preserving the quantum states in the coupled system; by contrast, strongly coupling the resonator directly to a classical measurement system typically causes rapid decoherence of these states.

Using the qubit, we demonstrate that the micromechanical resonator has been cooled to its ground state, and estimate that the maximum number of phonons in the relevant mechanical mode is $\langle n \rangle_{max} < 0.07$, implying that the resonator is in its ground state with a probability greater than 93%. We use our time-domain control of the qubit–resonator interaction to show further that we can controllably create an individual quantum excitation (a phonon) in the resonator, and observe the exchange of this quantized excitation between the resonator and the qubit. Moreover, we use a classical excitation to generate a coherent state in the resonator, which yields a qubit response that is in good agreement with theory. This demonstration provides strong evidence that quantum mechanics applies to a mechanical object large enough to be seen with the naked eye.

Mechanical resonator and quantum bit

We have chosen to use a micromechanical bulk dilatational resonator[25,26] with a fundamental dilatational resonance frequency of $f_r \approx 6$ GHz. We fabricate the resonator from a piezoelectric material so that the mechanical motion generates electrical signals, and vice versa. This electromechanical coupling allows us to measure the resonator using a quantum electrical circuit, a superconducting phase qubit. Qubits allow straightforward quantum-limited measurements of resonators[27,28], and here allow us to demonstrate unambiguously that the mechanical system can be cooled to its ground state as well as excited with individual mechanical quanta.

We first developed a method to fabricate the high-frequency mechanical resonator. The resonator is a film bulk acoustic resonator[25] comprising a thin film of aluminium nitride, which is a strong piezoelectric[29], sandwiched between two aluminium metal electrodes. The active part of the structure is mechanically suspended. The resonator responds to voltages by expanding or contracting in the direction perpendicular to the metal electrodes, with a fundamental resonance frequency of $f_r = v/2t$, where v is the average sound speed and t is the resonator thickness. An electron micrograph of a typical resonator, along with its equivalent electrical circuit and a classical resonance measurement, are shown in Fig. 1. Extensive experiments were made on a variety of mechanical resonators with this design to ensure that the resonance was indeed mechanical in nature; see Supplementary Information.

We co-fabricated the mechanical resonator and superconducting qubit on a single chip by first lithographically defining the mechanical

[1]Department of Physics, University of California, Santa Barbara, California 93106, USA.

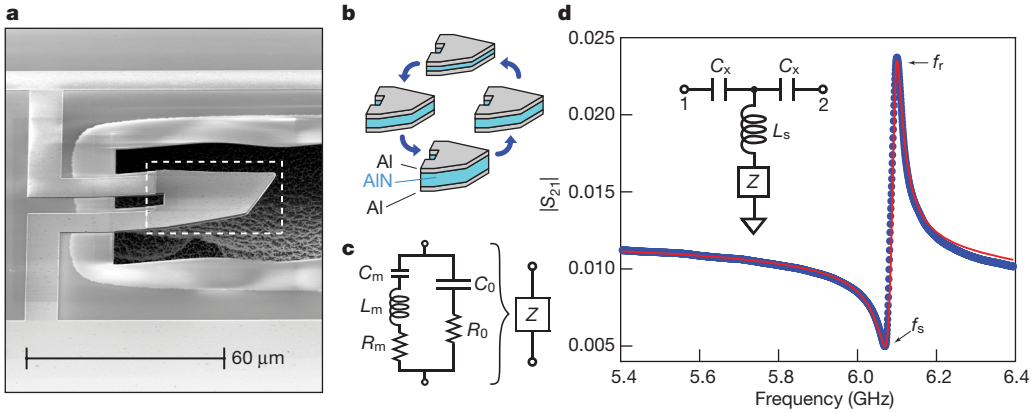

Figure 1 | Dilatational resonator. **a**, Scanning electron micrograph of a suspended film bulk acoustic resonator. Details on the fabrication of the resonator appear in Supplementary Information. The mechanical structure was released from the substrate by exposing the device to xenon difluoride, which isotropically etches any exposed silicon; the suspended structure comprises, from bottom to top, 150 nm SiO_2, 130 nm Al, 330 nm AlN and 130 nm Al. The dashed box indicates the mechanically active part of structure. **b**, Fundamental dilatational resonant mode for the mechanically active part of the resonator. The thickness of the structure changes through the oscillation cycle. **c**, Equivalent lumped-element circuit representation of the mechanical resonator, based on a modified van Dyke–Butterworth model[26,38]. This circuit includes a series-connected equivalent mechanical inductance L_m and capacitance C_m and a parallel geometric capacitance C_0, with mechanical dissipation modelled as R_m and dielectric loss as R_0. **d**, Measured classical transmission, $|S_{21}|$ (blue), and fit (red) of a typical mechanical resonance. The transmission has two features: one, at the frequency $f_s \approx 1/2\pi\sqrt{L_m C_m} \approx 6.07$ GHz, due to the series resonance of the equivalent mechanical components L_m and C_m, and one, at the slightly higher frequency $f_r \approx 1/2\pi\sqrt{L_m C_s} \approx 6.10$ GHz, due to L_m and the equivalent capacitance, C_s, of the capacitors C_m and C_0 in series. These expressions are approximate, as they do not take into account the effect of the dissipative elements and external circuit loading. Inset, equivalent circuit for the resonator (Z, as shown in **c**) embedded in the measurement circuit, including two on-chip external coupling capacitors with $C_x = 37$ fF and an inductive element with $L_s \approx 1$ nH that accounts for stray on-chip wiring inductance. Measurement is done using a calibrated network analyser that measures the transmission from port 1 to port 2. We calculate $C_0 = 0.19$ pF scaling from the geometry, and from the fit we obtain $C_m = 0.655$ fF, $L_m = 1.043$ μH, $R_m = 146\,\Omega$ and $R_0 = 8\,\Omega$. These values are compatible with the geometry and measured properties of AlN[29]. We calculate a mechanical quality factor of $Q \approx 260$ and a piezoelectric coupling coefficient of $k^2_{\mathrm{eff}} \approx 1.2\%$ (ref. 38).

structure and subsequently patterning the qubit. The fabrication process involved 13 layers of lithography, including metal and dielectric deposition and etching steps (Supplementary Information). In the last step, the device was exposed to xenon difluoride gas to release the mechanical resonator. A photomicrograph of a completed device is shown in Fig. 2.

Our quantum electrical circuit is a Josephson phase qubit[23,24,30] comprising a Josephson junction shunted in parallel by a capacitor and an inductor. The qubit can be approximated as a two-level quantum system with a ground state, $|g\rangle$, and an excited state, $|e\rangle$, separated in energy from $|g\rangle$ by ΔE, whose transition frequency, $f_q = \Delta E/h$, can be set between 5 and 10 GHz. The qubit frequency is precisely controlled by a current bias, which is applied using an external magnetic flux coupled through the parallel inductor. The state of the qubit is measured using a single-shot procedure[23]; accumulating ~1,000 such measurements allows us to determine the excited-state occupation probability, P_e (Supplementary Information). We have previously used the phase qubit to perform one- and two-qubit gate operations[24], to measure and quantum-control photons in an electromagnetic resonator[27,28] and to demonstrate the violation of a Bell inequality[31]. Here the qubit and the mechanical resonator are coupled through an interdigitated capacitor of capacitance $C_c \approx 0.5$ pF, to maximize the coupling strength between the qubit and resonator while not overloading the qubit. The coupled system can be modelled using the Jaynes–Cummings Hamiltonian[32], allowing us to estimate the coupling energy, g, between the mechanical resonator and the qubit. This energy involves the coupling capacitance as well as the electrical and mechanical properties of the mechanical resonator, as described in ref. 5; the corresponding coupling frequency is designed to be $\Omega = 2g/h \approx 110$ MHz. The equivalent electrical circuit for the combined resonator and qubit is shown in Fig. 2b.

Quantum ground state

The completed device was mounted on the mixing chamber of a dilution refrigerator and cooled to $T \approx 25$ mK. At this temperature, both the qubit and the resonator should occupy their quantum ground states. To study the cooled device, we performed microwave qubit spectroscopy[23] to reveal the resonant frequencies of the combined system, using the pulse sequence shown in Fig. 2c. We measured the excited-state probability, P_e, as a function of the qubit frequency and the microwave excitation frequency, as shown in Fig. 2d. The qubit frequency tunes as expected[23,30] and displays the characteristic level avoidance of a coupled system as its frequency crosses the fixed mechanical resonator frequency, f_r. Similar observations have been made using optomechanical systems[33].

We note that the mechanical resonator produces two features in the classical transmission measurement shown in Fig. 1d, generating a maximum (at f_r) and a minimum (at f_s) in the response. When coupled and measured using the qubit as in Fig. 2, the lower-frequency resonance, at f_s, does not produce a response, as this resonance does not correspond to a sustainable excitation of the complete circuit. However, the higher-frequency feature, at f_r, does sustain such excitations and thus appears in the spectroscopic measurement.

To determine the coupling strength between the qubit and the mechanical resonator, we fitted the detailed behaviour near the level avoidance, as shown in Fig. 2e. The fitted qubit–resonator coupling strength, $\Omega \approx 124$ MHz, corresponds to an energy transfer (Rabi-swap) time of about 4.0 ns, and is in reasonable agreement with our design value.

We then performed a second spectroscopy measurement, similar to the qubit spectroscopy but coupling the microwaves to the mechanical resonator through the capacitor of capacitance C_x shown in Fig. 2b, rather than to the qubit. In this measurement, shown in Fig. 3, the mechanical resonator acts as a narrow band-pass filter, so significant qubit excitation (large P_e) should only occur near the mechanical resonance frequency, f_r, as observed. In general, the spectrum looks very similar to that measured while exciting the qubit, providing strong support that the fixed resonance is indeed due to the mechanical resonator.

For higher-power microwave excitations, a new feature emerges in the resonator spectroscopy, as shown in Fig. 3b. The qubit, although approximated as a two-level system, actually has a double-well

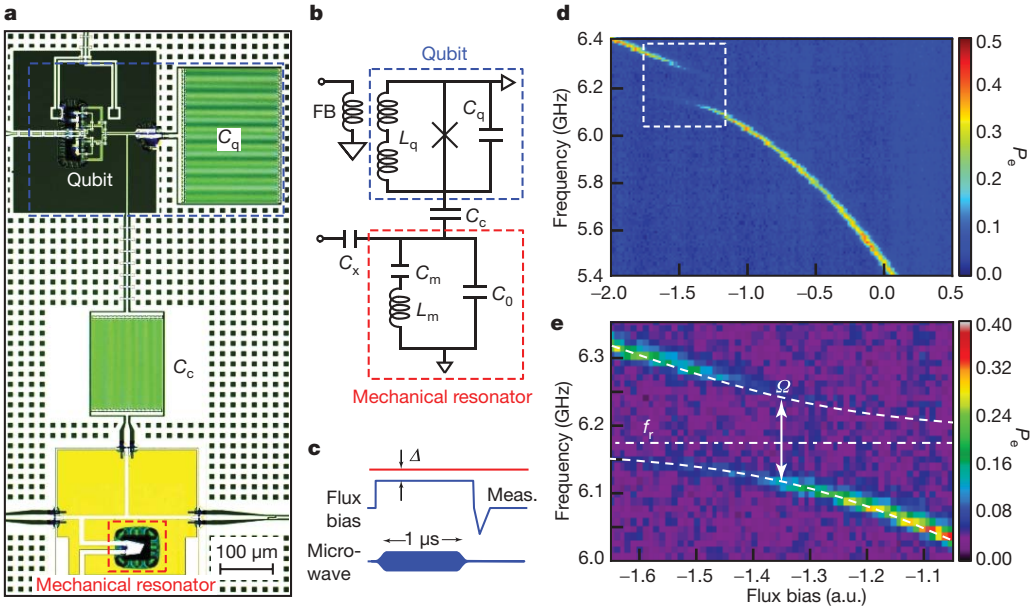

Figure 2 | Coupled qubit–resonator. **a**, Optical micrograph of the mechanical resonator coupled to the qubit (blemishes removed for clarity); fabrication details are in Supplementary Information. **b**, Circuit representation. The Josephson junction is represented by a cross, with parallel loop inductance L_q and capacitance C_q, the latter including the parallel combination of a 1-pF interdigitated shunting capacitor and the junction capacitance (not shown). The resonator has $C_0 = 0.2$ pF scaling from the geometry and the AlN thickness of 300 nm, with coupling capacitance $C_c \approx 0.5$ pF. The capacitor with $C_x = 0.5$ fF is used to couple external microwave signals to the resonator. The junction is modulated by magnetic flux applied through the flux-bias wire (FB), which controls the qubit $|g\rangle \leftrightarrow |e\rangle$ transition frequency. Microwave excitation of the qubit is also through FB. The shunting capacitor and the coupling capacitor C_c include a number of crossover shorting straps to eliminate potential electrical resonances. **c**, Qubit spectroscopy pulse sequence. The qubit (blue) is tuned to within $\Delta = f_q - f_r$ of the resonator (red) and a 1-μs microwave tone is applied to the qubit; the qubit state is then measured (Meas.) in a single-shot manner using a flux-bias pulse, from which the excited-state probability, P_e, is evaluated. **d**, Qubit spectroscopy, showing P_e as a function of qubit frequency (expressed in terms of flux bias) and microwave frequency. The qubit frequency behaves as expected, with a prominent splitting as the qubit is tuned through the resonator frequency, $f_r = 6.17$ GHz. a.u., arbitrary units. **e**, Enlarged view of the dashed box in **d**. The horizontal dash–dot line shows the resonator frequency, f_r, and the dashed lines show the fit to the coupled mode frequencies, with fitted coupling frequency $\Omega = 2g/h \approx 124$ MHz.

potential with a small number of states in the left-hand well, the two lowest being the qubit states $|g\rangle$ and $|e\rangle$, separated from the right-hand well by a barrier whose height changes with flux bias. When the mechanical resonator is driven on resonance at higher excitation powers, there is sufficient energy to excite the qubit over the barrier and into the right-hand well, yielding a large value for P_e even when the qubit energy-level spacing is not resonant with the resonator. This effect is pronounced at higher positive flux bias, for which the left-hand well is shallower, and generates the distinct horizontal line in the right-hand panel of Fig. 3b. From this line, we obtain a precise determination of the resonator frequency, $f_r = 6.175$ GHz. We note further that the resonator frequency seen in this higher-power measurement agrees with that revealed in the lower-power measurement, as expected for a harmonic response.

These spectroscopic measurements are useful in probing the resonant modes of our circuit. However, although the qubit is a quantum device, the measurement is essentially classical, revealing little about the quantum behaviour of the mechanical resonator. We therefore performed an additional experiment, using the qubit to probe the energy state of the resonator when no microwave signal was applied—essentially using the qubit as a quantum thermometer. This allowed us to verify with high precision that the resonator is actually in its ground state.

We initially prepared the qubit in its ground state, $|g\rangle$, with a $|g\rangle \leftrightarrow |e\rangle$ transition frequency of 5.44 GHz, which is well out of resonance with the resonator and effectively turns off the qubit–resonator interaction. We then applied a flux-bias pulse to bring the qubit to within $\Delta = f_q - f_r$ of the resonator frequency, and kept the qubit at this frequency for 1 μs. After returning the qubit to its original frequency, we measured the excited-state probability, P_e, as shown in Fig. 4. The qubit remains in its ground state for all values of Δ, with no detectable increase in P_e from its baseline value of 4%, even at resonance ($\Delta = 0$). In Fig. 4, we also display numerical predictions for the expected qubit P_e for a range of resonator phonon occupations, $\langle n \rangle$. The expected response has a peak near zero detuning and exceeds the measured response by a substantial amount even for small $\langle n \rangle$. We obtain a very conservative upper limit for the thermal occupation, $\langle n \rangle_{max} < 0.07$ (Supplementary Information).

As a check, we performed the same experiment but, just before measuring the qubit, applied a microwave pulse to swap the populations of the qubit states $|g\rangle$ and $|e\rangle$. After this swap, the probability P_e is about 92%, independent of Δ, again demonstrating negligible additional excitation of the qubit; a little additional excitation would cause P_e to decrease near $\Delta = 0$.

This null result demonstrates that the resonator phonon occupation, $\langle n \rangle$, is much less than one; that is, the resonator is with high probability in its quantum ground state.

Quantum excitations

We next used our time-domain control of the qubit to create and measure individual quantum excitations in the resonator, allowing us then to measure the resonator's single-excitation energy relaxation time and phase coherence time. We first characterized the qubit's energy relaxation time, T_{1q}, using the standard Rabi decay technique[23], described in detail in Supplementary Information. From this measurement, we find that $T_{1q} \approx 17$ ns. This is significantly less than the time for our typical qubits[31], $T_{1q} \approx 500$ ns, which we attribute here to dielectric dissipation in the aluminium nitride and the device substrate[34].

Despite the relatively small T_{1q}, the qubit coherence time was sufficient for us to perform quantum operations on the resonator. The coupling strength between the qubit and the resonator was fixed at $\Omega = 2g/h \approx 124$ MHz, as discussed above. When the qubit and the resonator are tuned on-resonance, energy will be exchanged

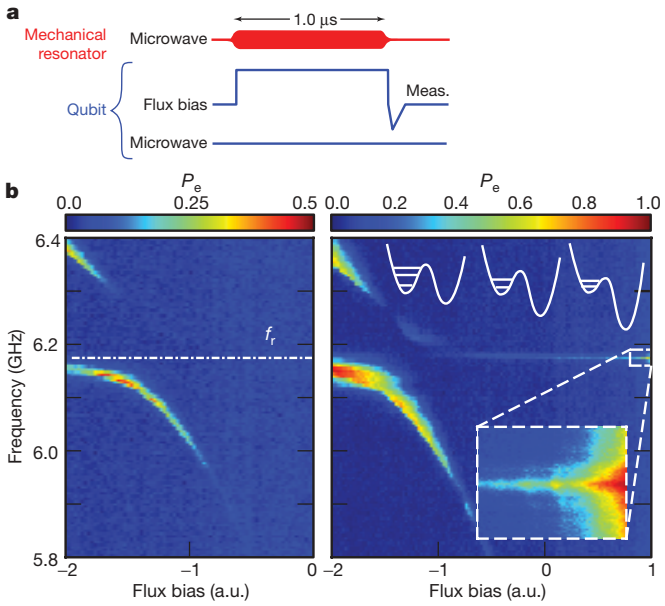

Figure 3 | Resonator spectroscopy. a, Pulse sequence applied to the qubit (blue) and the mechanical resonator (red). The qubit is tuned to within Δ of the resonator frequency and a 1-μs microwave tone is applied to the resonator through C_x. The resulting qubit P_e is then evaluated. **b**, Left: spectroscopic P_e as a function of qubit flux bias and applied microwave frequency. Right: same as left-hand panel but with higher microwave power, showing qubit state ejection due to interaction with a highly excited mechanical resonator. The structure of the qubit well levels is indicated schematically as a function of flux bias, showing marginal excited-state confinement at higher positive flux bias. Inset, detail at the highest flux bias, for which the left-hand well is very shallow, highlighting qubit ejection at the resonant frequency of the mechanical resonator.

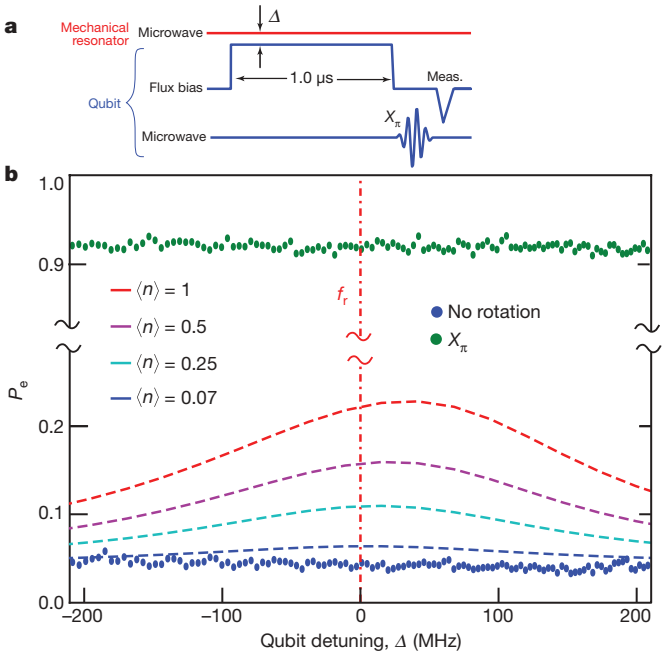

Figure 4 | Qubit thermometry of resonator. a, Pulse sequence. The qubit in its ground state is tuned to within Δ of the resonator frequency for 1 μs, and in one set of measurements its excited-state probability, P_e, is then measured. In another set of measurements, a microwave swap pulse (X_π) was applied to the qubit before measurement, exchanging the $|g\rangle$ and $|e\rangle$ populations, and followed with a measurement of P_e. The detuning, Δ, was scanned over the range −210–+210 MHz. **b**, Excited-state probability, P_e, with (green) and without (blue) the X_π pulse, as a function of detuning, Δ. The mechanical resonance at f_r ($\Delta = 0$) is marked by the vertical dash–dot line, and the dashed lines are the numerically calculated values of P_e for different resonator mean phonon occupations, $\langle n\rangle$ (Supplementary Information); the shift in peak response from $\Delta = 0$ for larger values of $\langle n\rangle$ is due to the higher energy levels in the qubit, which come into resonance for $\Delta > 0$. We note that, in the experiment, the resonator does not excite the qubit from its ground state, indicating that the resonator itself is in the ground state.

(swapped) between the two at this frequency, with unit probability. When the qubit is detuned from the resonator by a frequency $\Delta = f_q - f_r$, the swap frequency increases to $\sqrt{\Omega^2 + \Delta^2}$ but the transfer probability should be reduced to $\Omega^2/(\Omega^2 + \Delta^2)$.

We generated an excitation in the resonator by first exciting the qubit and then swapping the excitation to the resonator, using the pulse sequence shown in Fig. 5a. The qubit was excited from $|g\rangle$ to $|e\rangle$ with a π-pulse while the qubit was at its resting frequency of 5.44 GHz, detuned by $\Delta = -735$ MHz from the resonator. We then increased the qubit frequency towards the resonator frequency, performing the experiment for interaction detunings, Δ, ranging from −150 MHz to +90 MHz. After a variable delay, the qubit was returned to its resting frequency and its excited-state probability, P_e, was measured. This response was mapped out as a function of delay, τ, and detuning, Δ, yielding the data in Fig. 5b (left, simulated data; right, experimental data). Experiment and simulation are in good agreement. When the qubit frequency is close to that of the resonator, we observe oscillations in $P_e(\tau)$. The oscillation period is longest at resonance ($\Delta = 0$) and shortest at the largest values of $|\Delta|$, as anticipated; we fit the sequence of local maxima in P_e, as a function of τ and Δ, to the expected Lorentzian dependence of the swap period, as shown by the dash–dot lines in Fig. 5b. The corresponding minimum swap frequency is found to be $\Omega = 132$ MHz, which is close to that determined from spectroscopy.

The amplitudes of the swap oscillations in P_e for $\Delta < 0$ are seen to be smaller than the corresponding amplitudes for $\Delta > 0$, not displaying the expected symmetric dependence of the transfer probability. This is due to the non-zero rise and fall times (~1 ns) of the frequency-tuning pulse, which yields a higher swap efficiency for larger values of Δ. The qubit–resonator swap is initiated as the tuning pulse brings the qubit towards the resonator, swapping some of the qubit excitation into the resonator before the qubit is at the interaction frequency, and further continuing the swap when the qubit is returning to its resting frequency. This causes an interference that affects the swap visibility, with a reduction for small values of Δ, where the frequency tuning is proportionally more adiabatic than for larger values of Δ. Hence, the exchange probability is maximized[35,36] for larger values of Δ. The simulations, which use trapezoidal tuning pulses to approximate the experiment, support this explanation; see Supplementary Information.

In Fig. 5c, we show $P_e(\tau)$ for the interaction frequency indicated by the white dashed line in Fig. 5b. Five complete cycles are visible; each minimum corresponds to a transfer of the excitation from the qubit to the resonator and each maximum corresponds to a return of the excitation from the resonator to the qubit, with decay due to dissipation (see below). At $\tau = 0$, the system is in the state $|e0\rangle$, where the first state vector element represents the qubit and the second represents the resonator. After one-quarter of the first Rabi oscillation, at $\tau \approx 1.9$ ns, the qubit and the mechanical resonator are entangled in the state $|g1\rangle + |e0\rangle$. At $\tau = \tau_{ph} \approx 3.8$ ns, the qubit state has been completely transferred to the mechanical resonator, generating a single phonon and leaving the system in the state $|g1\rangle$. After a full Rabi period, at $\tau = 2\tau_{ph} \approx 7.6$ ns, the excitation is transferred back to the qubit, returning the system to the state $|e0\rangle$, with the resonator in its ground state.

The data shown in Fig. 5 provide clear and compelling evidence that we have created a single quantum excitation in a macroscopic mechanical object, and that the system's quantum coherence is sufficient to allow us to transfer this excitation multiple times between the qubit and the mechanical resonator. In this process, the system exists at times in an entangled qubit–resonator quantum state.

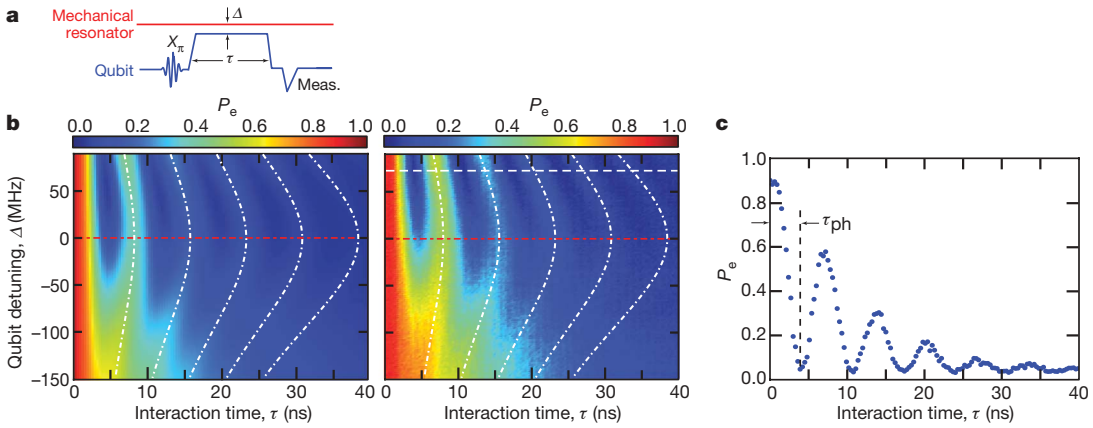

Figure 5 | Qubit–resonator swap oscillations. a, Pulse sequence used to generate quantum state exchange between the qubit and the resonator. The qubit is initially in the ground state, $|g\rangle$, at its resting frequency of 5.44 GHz, and is excited to the state $|e\rangle$ by a microwave π-pulse (X_π). The qubit is then tuned to within $\Delta = f_q - f_r$ of the resonator and kept there for a time τ. After returning the qubit to its resting frequency, we evaluate its excited-state probability, P_e. The pulse sequence is shown using a compressed format in which the flux bias and the microwave excitation are combined. **b**, Qubit excited-state probability, P_e, as a function of interaction time, τ, and detuning, Δ, showing state transfer between the qubit and the resonator, in which a qubit excitation is exchanged with a phonon in the mechanical resonator (left, simulations; right, experiment). The red dash–dot line is at the resonator frequency, f_r. **c**, Data along the white dashed line in **b**, corresponding to a fixed detuning of $\Delta = 72$ MHz (the value with the highest visibility swaps). Maxima correspond to the qubit being in its excited state and minima correspond to state transfer to the resonator, creating a single phonon. The swap time needed to generate one phonon is $\tau_{ph} \approx 3.8$ ns. The nearly complete swaps for $\Delta > 0$ are due to the time dependence of the tuning pulse and the resulting complicated dynamics, as borne out by simulations; see Supplementary Information.

Using the ability to generate a single phonon, we next determined the resonator's energy relaxation time, T_{1r}, by injecting a single phonon into the resonator and measuring its decay, as shown in Fig. 6a, b. A fit to the results yields a resonator energy relaxation time of $T_{1r} \approx 6.1$ ns, in reasonable agreement with the decay time, $Q/2\pi f_r \approx 6.7$ ns, expected from the classically measured quality factor, $Q \approx 260$.

We also attempted to measure the resonator's dephasing time, T_{2r}, as shown in Fig. 6c, d. This measurement was performed using a Ramsey-fringe experiment, with the dephasing time revealed by the evolution of the state $|g0\rangle + |g1\rangle$, which is a quantum superposition of the state in which the resonator contains zero phonons and the state in which it contains one phonon. The fitted dephasing time is $T_{2r} \approx 20$ ns, which is anomalously longer than the expected maximum, $2T_{1r} \approx 12$ ns. However, this measurement is relatively complex, requiring several pulses with good pulse control, and errors can result in longer-than-expected dephasing times; what we can conclude from this measurement is that pure dephasing is not a dominant decay in and of itself.

To illustrate the resonator's bosonic nature, we also performed measurements in which we directly excited the mechanical resonator with a classical microwave pulse. With the qubit at its resting frequency, we applied a variable-amplitude Gaussian pulse to the resonator. The qubit was then brought into resonance with the resonator ($\Delta = 0$) and held there for an interaction time τ. Finally, the qubit was returned to its resting frequency and P_e was measured. This probability is shown in Fig. 7 as a function of the Gaussian pulse amplitude and τ, along with the results of a quantum simulation (Supplementary Information). As the microwave amplitude is increased, the frequency of the oscillations in $P_e(\tau)$ increases. This is a clear indication of the bosonic nature of the resonator, as the swap frequency between the qubit and the mechanical resonator is proportional to the square root of the number of phonons in the

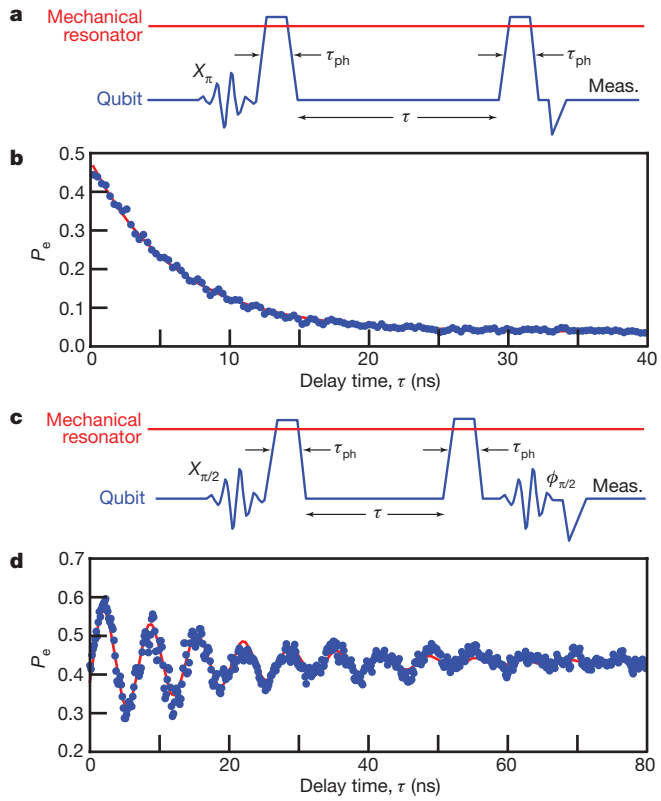

Figure 6 | Resonator energy decay and dephasing times. a, Pulse sequence used to inject one phonon into the resonator and measure its decay. The qubit is first excited from $|g\rangle$ to $|e\rangle$ while at its resting frequency, using a microwave π-pulse. It is then tuned to the interaction frequency of 6.25 GHz ($\Delta = 72$ MHz, the detuning chosen for the highest visibility swaps), and left there for a time τ_{ph}, transferring a phonon to the resonator and leaving the qubit in its ground state. After returning the qubit to its resting frequency for a delay time τ, it is brought back to the interaction frequency for a time τ_{ph}, transferring any remaining excitation back to the qubit. The excited-state probability, P_e, is then evaluated. **b**, Measured $P_e(\tau)$, showing the exponential decrease of the single-phonon state (blue points). We fit a resonator energy relaxation time of $T_{1r} \approx 6.1$ ns (red line). **c**, Pulse sequence used to measure the resonator phase coherence time. The sequence is similar to that in **a**, except we replace the initial π-pulse with a π/2-pulse ($X_{\pi/2}$) to excite the qubit state $|g\rangle + |e\rangle$, and after the second resonator transfer apply a second π/2-pulse ($\phi_{\pi/2}$) before measuring P_e, thus performing a Ramsey-fringe measurement. The phase of the second π/2-pulse is swept at a rate that determines the frequency of the resulting oscillations. **d**, Measured $P_e(\tau)$, showing dephasing in the mechanical resonator (blue dots) and a fit (red line) using a dephasing time of $T_{2r} \approx 20$ ns.

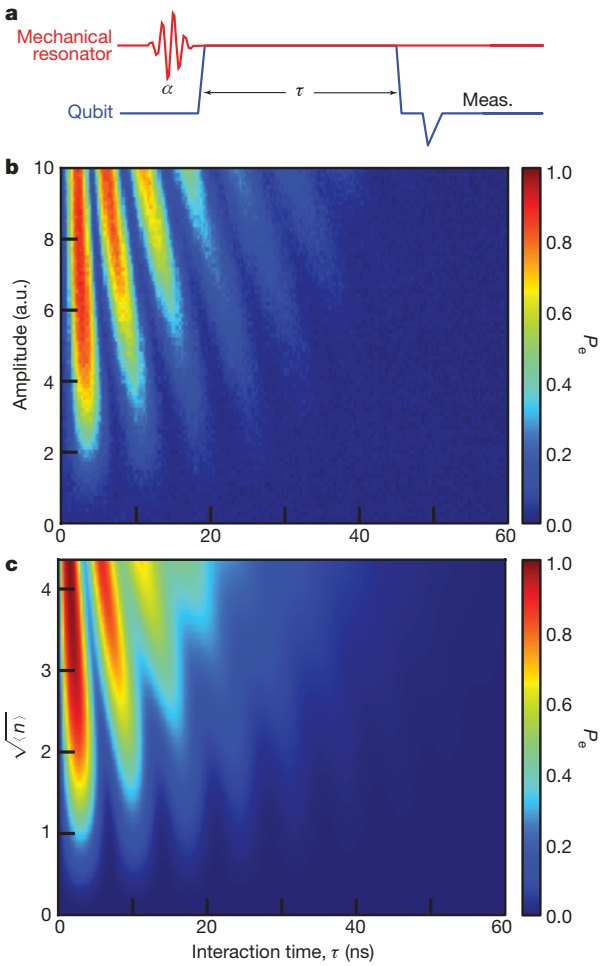

Figure 7 | Resonator coherent state. a, Pulse sequence to generate coherent phonon states. With the qubit at its resting frequency, an on-resonance Gaussian pulse of fixed duration (5.0 ns) and variable amplitude is applied to the resonator. The qubit is then tuned to $\Delta = 0$ and left for an interaction time τ; the qubit excited-state probability, P_e, is then evaluated. **b**, Measured P_e as a function of pulse amplitude and interaction time, τ. **c**, Simulation of coherent state evolution, with P_e expressed as a function of τ and $\sqrt{\langle n \rangle}$, $\langle n \rangle$ being the mean number of injected phonons; see Supplementary Information.

resonator[27,28,37]; comparison with the simulation shows good agreement. We note that there was little or no direct microwave excitation of the qubit, as for small interaction times, τ, the qubit was always measured to be in its ground state. We further note that if the resonator were instead behaving as a few-level quantum system, simulations demonstrate that the measured response would be markedly different; this provides good evidence that the resonator here is behaving as a harmonic system.

The results we report here provide strong evidence that we have achieved reasonable quantum control over a macroscopic mechanical system. We note that full Wigner tomography of the resonator states, revealing quantum phase coherence for the entangled states[28], would provide further strong evidence of quantum behaviour in this system; however, the resonator lifetime, T_{1r}, is too short, in comparison with the state preparation and measurement times, to permit such an analysis.

METHODS SUMMARY

The mechanical resonator, which was made of aluminium nitride and aluminium, and the qubit, superconducting quantum interference device (SQUID) and superconducting wiring, which were made of aluminium, were fabricated on an oxidized silicon wafer using standard semiconductor processing. We diced the wafer into 6.25 mm × 6.25 mm chips and placed one chip in an aluminium mount, using wire-bonded electrical connections. We made measurements of the resonator, shown in Fig. 1, at room temperature (~293 K) using a commercial microwave network analyser, and made qubit measurements of the resonator using a custom-built dilution refrigerator. The device mount was attached to the mixing chamber of the dilution refrigerator, and the device operated in vacuum at a temperature of 25 mK. Measurement cabling from outside the cryostat to the device was heavily filtered and attenuated. We generated microwave signals using a commercial microwave synthesizer, and controlled their amplitudes and frequencies using an I/Q modulator. Control signals for the modulator were generated using a high-speed digital-to-analogue converter, controlled by a computer. The qubit bias and SQUID bias were generated using custom electronics controlled by computer via fibre-optic lines. The SQUID measurement output was amplified and transmitted via fibre-optics to the same computer. Typical measurements of the excited state probability, P_e, involved accumulating on the order of 1,000 separate single-shot measurements. Full details may be found in Supplementary Information.

Received 19 November 2009; accepted 1 March 2010.
Published online 17 March 2010.

1. Braginsky, V. B. & Khalili, F. Y. *Quantum Measurement* (Cambridge Univ. Press, 1992).
2. Courty, J. M., Heidmann, A. & Pinard, M. Quantum limits of cold damping with optomechanical coupling. *Eur. Phys. J. D* **17,** 399–408 (2001).
3. Armour, A. D., Blencowe, M. P. & Schwab, K. C. Entanglement and decoherence of a micromechanical resonator via coupling to a Cooper-pair box. *Phys. Rev. Lett.* **88,** 148301 (2002).
4. Knobel, R. G. & Cleland, A. N. Nanometre-scale displacement sensing using a single electron transistor. *Nature* **424,** 291–293 (2003).
5. Cleland, A. N. & Geller, M. R. Superconducting qubit storage and entanglement with nanomechanical resonators. *Phys. Rev. Lett.* **93,** 070501 (2004).
6. LaHaye, M. D., Buu, O., Camarota, B. & Schwab, K. C. Approaching the quantum limit of a nanomechanical resonator. *Science* **304,** 74–77 (2004).
7. Blencowe, M. Quantum electromechanical systems. *Phys. Rep.* **395,** 159–222 (2004).
8. Martin, I., Shnirman, A., Tian, L. & Zoller, P. Ground-state cooling of mechanical resonators. *Phys. Rev. B* **69,** 125339 (2004).
9. Kleckner, D. & Bouwmeester, D. Sub-kelvin optical cooling of a micromechanical resonator. *Nature* **444,** 75–78 (2006).
10. Blencowe, M. P. & Buks, E. Quantum analysis of a linear dc SQUID mechanical displacement detector. *Phys. Rev. B* **76,** 014511 (2007).
11. Schliesser, A., Riviere, R., Anetsberger, G., Arcizet, O. & Kippenberg, T. J. Resolved-sideband cooling of a micromechanical oscillator. *Nature Phys.* **4,** 415–419 (2008).
12. Regal, C. A., Teufel, J. D. & Lehnert, K. W. Measuring nanomechanical motion with a microwave cavity interferometer. *Nature Phys.* **4,** 555–560 (2008).
13. LaHaye, M. D., Suh, J., Echternach, P. M., Schwab, K. C. & Roukes, M. L. Nanomechanical measurements of a superconducting qubit. *Nature* **459,** 960–964 (2009).
14. Gigan, S. *et al.* Self-cooling of a micromirror by radiation pressure. *Nature* **444,** 67–70 (2006).
15. Arcizet, O., Cohadon, P.-F., Briant, T., Pinard, M. & Heidmann, A. Radiation-pressure cooling and optomechanical instability of a micromirror. *Nature* **444,** 71–74 (2006).
16. Wilson-Rae, I., Nooshi, N., Zwerger, W. & Kippenberg, T. J. Theory of ground-state cooling of a mechanical oscillator using dynamical backaction. *Phys. Rev. Lett.* **99,** 093901 (2007).
17. Marquardt, F., Chen, J. P., Clerk, A. A. & Girvin, S. M. Quantum theory of cavity-assisted sideband cooling of mechanical motion. *Phys. Rev. Lett.* **99,** 093902 (2007).
18. Thompson, J. D. *et al.* Strong dispersive coupling of a high-finesse cavity to a micromechanical membrane. *Nature* **452,** 72–75 (2008).
19. Gröblacher, S. *et al.* Demonstration of an ultracold micro-optomechanical oscillator in a cryogenic cavity. *Nature Phys.* **5,** 485–488 (2009).
20. Park, Y. S. & Wang, H. Resolved-sideband and cryogenic cooling of an optomechanical resonator. *Nature Phys.* **5,** 489–493 (2009).
21. Schliesser, A., Arcizet, O., Riviere, R., Anetsberger, G. & Kippenberg, T. J. Resolved-sideband cooling and position measurement of a micromechanical oscillator close to the Heisenberg uncertainty limit. *Nature Phys.* **5,** 509–514 (2009).
22. Rocheleau, T. *et al.* Preparation and detection of a mechanical resonator near the ground state of motion. *Nature* **463,** 72–75 (2010).
23. Steffen, M. *et al.* State tomography of capacitively shunted phase qubits with high fidelity. *Phys. Rev. Lett.* **97,** 050502 (2006).
24. Martinis, J. M. Superconducting phase qubits. *Quantum Inf. Process.* **8,** 81–103 (2009).
25. Ruby, R. C., Bradley, P., Oshmyansky, Y., Chien, A. & Larson, J. D. III. in *Proc. 2001 IEEE Ultrasonics Symp.* (eds Yuhas, D. E. & Schneider, S. C.) 813–821 (IEEE, 2001).
26. Nam, K. *et al.* Piezoelectric properties of aluminum nitride for thin film bulk acoustic wave resonator. *J. Korean Phys. Soc.* **47,** S309–S312 (2005).
27. Hofheinz, M. *et al.* Generation of Fock states in a superconducting quantum circuit. *Nature* **454,** 310–314 (2008).

28. Hofheinz, M. *et al.* Synthesizing arbitrary quantum states in a superconducting resonator. *Nature* **459,** 546–549 (2009).
29. Ambacher, O. Growth and applications of group-III nitrides. *J. Phys. D* **31,** 2653–2710 (1998).
30. Clarke, J., Cleland, A. N., Devoret, M. H., Esteve, D. & Martinis, J. M. Quantum mechanics of a macroscopic variable: the phase difference of a Josephson junction. *Science* **239,** 992–997 (1988).
31. Ansmann, M. *et al.* Violation of Bell's inequality in Josephson phase qubits. *Nature* **461,** 504–506 (2009).
32. Haroche, S. & Raimond, J.-M. *Exploring the Quantum: Atoms, Cavities and Photons* (Oxford Univ. Press, 2006).
33. Gröblacher, S., Hammerer, K., Vanner, M. R. & Aspelmeyer, M. Observation of strong coupling between a micromechanical resonator and an optical cavity field. *Nature* **460,** 724–727 (2009).
34. O'Connell, A. D. *et al.* Microwave dielectric loss at single photon energies and millikelvin temperatures. *Appl. Phys. Lett.* **92,** 112903 (2008).
35. Shytov, A. V., Ivanov, D. A. & Feigelman, M. V. Landau-Zener interferometry for qubits. *Eur. Phys. J. B* **36,** 263–269 (2003).
36. Oliver, W. D. *et al.* Mach-Zehnder interferometry in a strongly driven superconducting qubit. *Science* **310,** 1653–1657 (2005).
37. Schuster, I. *et al.* Nonlinear spectroscopy of photons bound to one atom. *Nature Phys.* **4,** 382–385 (2008).
38. Larson, J. D. III, Bradley, P. D., Warternberg, S. & Ruby, R. C. in *Proc. 2000 IEEE Ultrasonics Symp.* (eds Schneider, S. C., Levy, M. & McAvoy, B. R.) 863–868 (IEEE, 2000).

Supplementary Information is linked to the online version of the paper at www.nature.com/nature.

Acknowledgements We would like to thank M. Geller for numerous conversations and A. Berube for assistance with resonator fabrication and measurements. This work was supported by the US National Science Foundation (NSF) under grant DMR-0605818 and by the Intelligence Advanced Research Projects Activity under grant W911NF-04-1-0204. Devices were made at the University of California, Santa Barbara, Nanofabrication Facility, which is part of the NSF-funded US National Nanotechnology Infrastructure Network.

Author Contributions A.D.O'C. fabricated the devices and performed the measurements, M.H. providing measurement assistance. A.N.C., A.D.O'C. and J.M.M. conceived and designed the experiment. All authors contributed to providing experimental support and writing the manuscript.

Author Information Reprints and permissions information is available at www.nature.com/reprints. The authors declare no competing financial interests. Correspondence and requests for materials should be addressed to A.N.C. (anc@physics.ucsb.edu).